Edge-driven Image Interpolation using Adaptive Anisotropic Radial Basis Functions

G. Casciola · L.B. Montefusco · S. Morigi

Abstract This paper investigates the image interpolation problem, where the objective is to improve the resolution of an image by dilating it according to a given enlargement factor. We present a novel interpolation method based on Radial Basis Functions (RBF) which recovers a continuous intensity function from discrete image data samples. The proposed anisotropic RBF interpolant is designed to easily deal with the local anisotropy in the data, such as edge-structures in the image. Considering the underlying geometry of the image, this algorithm allows us to remove the artifacts that may arise when performing interpolation, such as blocking and blurring. Computed examples demonstrate the effectiveness of the method proposed by visual comparisons and quantitative measures.

Keywords Radial basis function · Image interpolation · Image enlargement · Structure tensor

1 Introduction

A classical problem in image processing is the interpolation of images: given an image, the problem is to find a visually pleasing enlargement of it without creating checkerboard edges or smearing out the details. Applications of image interpolation techniques range from digital photography

G. Casciola · L.B. Montefusco · S. Morigi (✉)
Department of Mathematics, University of Bologna,
P.zza di Porta San Donato 5, 40127 Bologna, Italy
e-mail: morigi@dm.unibo.it

L.B. Montefusco
e-mail: montelau@dm.unibo.it

G. Casciola
e-mail: casciola@dm.unibo.it

to video surveillance, satellite image analysis, computer vision, computer graphics, medical imaging, and many other important fields. Depending on the application and user, the interpolation process can be applied to have the ability to zoom in on a specific part of the image, or just to obtain high resolution images from a single low-resolution image.

Knowing image intensities at a discrete grid, the interpolation process fits a continuous bivariate function to these discrete data and estimates the surface values at an arbitrary high resolution grid to determine the intensity of the high resolution image.

Let the function $f : \Omega \to \mathbb{R}$ be our ideal continuous image, defined over a rectangular domain $\Omega \in \mathbb{R}^2$. The image U is a discrete sampling of f at a lattice of Ω. For computation purposes, we can think of this lattice as a uniform grid of positive integers of resolution $n_1 \times n_2$. Given the low-resolution image U and a factor $s = (s_1, s_2)$, $s_1, s_2 > 1$, the interpolation process produces the high resolution image V of resolution $N_1 \times N_2$, where $N_1 = s_1 n_1$ and $N_2 = s_2 n_2$. We will refer to s as the magnification factor.

There are two types of interpolation methods: linear and nonlinear ones.

In the simplest linear approach the function f is assumed to be reconstructed by a convolution kernel $\phi : \mathbb{R}^2 \to \mathbb{R}$, so that f can be approximated by

$$f \simeq U * \phi. \tag{1}$$

Several interpolation kernels of finite size have been introduced in the literature, as the approximation of the ideal interpolation kernel (*sinc* function), which is spatially unlimited. In the discrete setting, the convolution (1) corresponds to a linear interpolation filter. Linear filters differ in the choice of ϕ, which essentially determines how to compute the weighted average of nearby pixels. Three of the simplest

linear filters are the nearest-neighbor, bilinear and bicubic interpolations, which involve a small number of pixel values and are very fast. For an exhaustive survey, we refer the reader to [13]. However, most of the linear interpolation methods fail to capture the edges of the image, and consequently generate interpolated images with ringing artifacts and jagged aliasing effects along the edges.

A better comprehension of this behavior is obtained by investigating the spectral contents of images interpolated by linear algorithms in the frequency domain. The linear algorithms cannot correctly estimate the missing high-frequency information, which represents the edge structures in the image domain. The high frequency components are simply suppressed, while the low ones are preserved. This leaves an image that is essentially blurred around its edges.

It is well-known that taking edge information into account improves the interpolated image quality since the human visual perception system makes significant use of edges. In order to overcome the artifacts of linear methods, several nonlinear methods have been introduced, which instead of simply interpolating the discrete data, consider the underlying geometry of the image. These edge-driven methods provide a significant improvement in the visual quality by using interpolation which preserves the edge information. In one of the earliest papers proposed to reduce edge artifacts, Jensen and Anastassiou [10] propose to estimate the orientation of each edge in the image by using projections onto an orthonormal basis and the interpolation process is modified to avoid interpolating across the edges. An estimate of the high-resolution edge map to iteratively correct the interpolated pixels has been introduced in [1]. Another interesting approach called data dependent triangulation [18] performs interpolation by dividing every four-pixel square into two triangles and restricts interpolation within the triangles. Hwang et al. in [9] use an adaptive image interpolation approach based on local gradient features. Li et al. in [14] propose an edge-directed interpolation which uses an estimate of the local covariance characteristics at low resolution. In [19] the edges are enhanced and interpolated by using a quadratic Volterra filter. Guichard et al. in [8] successfully extended a regularized total variation approach to the problem of image zooming. Nonlinear methods also include edge-forming methods that rely on PDE-based diffusion techniques, see [6, 11, 15]. Other effective methods have been proposed which perform interpolation in a transform (e.g. wavelet) domain [2]. These algorithms assume the low-resolution image to be the lowpass output of the wavelet transform and utilize dependence across wavelet scales to predict the missing coefficients in the more detailed scales.

We propose a new adaptive algorithm for image interpolation which integrates edge detection information into an RBF anisotropic interpolation process. More precisely, we extract the local characteristics from the pixel neighborhood at the low-resolution image using a structure tensor, which induces a characteristic metric for each pixel. Previous approaches to edge-directed interpolation quantize the edge orientation into a finite number of choices (e.g. horizontal, vertical or diagonal) thus affecting the accuracy of the imposed edge model [7]. Instead, we replace the Euclidean metric with the new one and this gives rise to local anisotropic RBF interpolants, which are able to continuously adapt their shape according to the pixel metric. We use the new metric to tune both the shape of the anisotropic RBFs and the support of the local RBF interpolant to match an arbitrary oriented edge. A global adaptive RBF interpolation scheme is then able to reconstruct the image by suitably combining the local contributions.

A global RBF anisotropic interpolation scheme of this type has been proposed in [4, 5] and applied to the reconstruction of implicit surfaces from clouds of points. In that context the surface structures, such as edge, corner or flat regions, were detected by local covariance structures. When the data is uniformly distributed on a grid, as in the image interpolation case, it is more natural to use the structure tensor to estimate the edge orientations in the image.

The isotropic version of the global RBF interpolation scheme, where the classical Euclidean metric is used, has been successfully introduced in [3] for the reconstruction of a surface from bivariate scattered data. When applied to uniform data grids, this method can be considered a convolution-based approach to image interpolation and, as such, it presents all the drawbacks of the linear approaches to image interpolation.

In the remaining part of this section we introduce the basic RBF interpolation problem, which is used in Sect. 3 to discuss the proposed interpolation algorithm.

The radial basis function interpolant F of a given function $f \in C(\mathbb{R}^d)$, on a set $X = \{\mathbf{x}_i \in \mathbb{R}^d\}_{i=1,\ldots,N} \subseteq \mathbb{R}^d$ of distinct points, is given by

$$F(\mathbf{x}) = \sum_{j=1,\ldots,N} c_j \varphi(\|\mathbf{x} - \mathbf{x}_j\|_2), \qquad (2)$$

where $\varphi : \mathbb{R}^d \to \mathbb{R}$ is a radial function, and the coefficients are determined by the interpolation conditions

$$F(\mathbf{x}_j) = f(\mathbf{x}_j), \quad j = 1, \ldots, N. \qquad (3)$$

Interpolants of the form (2) require that the functions φ belong to a special class of positive definite radial basis functions. Examples of positive definite RBFs of order 0 are the inverse multiquadric RBF

$$\varphi(r) = (r^2 + \gamma^2)^{-\frac{1}{2}} \qquad (4)$$

and the Gaussian RBF defined as

$$\varphi(r) = e^{-\frac{r^2}{\alpha}}, \qquad (5)$$

with shape parameters $\gamma > 0$ and $\alpha > 0$ respectively. The interpolation problem (3), rewritten in matrix-vector form as

$$A\mathbf{c} = \mathbf{f} \tag{6}$$

is uniquely solvable since the interpolation matrix $A = (\varphi(\|\mathbf{x}_i - \mathbf{x}_j\|_2))$, $1 \leq i, j \leq N$ is positive definite.

Since the reconstruction quality depends on the density of the centers $\mathbf{x}_j$, a commonly used density-measure for a set of points X is known as *fill distance* and is defined as

$$h_r(\mathbf{x}) = \max_{\mathbf{x} \in J_r(x)} \min_{1 \leq i, j \leq N} \|\mathbf{x} - \mathbf{x}_j\|_2 \tag{7}$$

where $J_r(\mathbf{x}) = \{\mathbf{y} \in \mathbb{R}^d / \|\mathbf{y} - \mathbf{x}\|_2 \leq r\}$, for some fixed r.

The rest of the paper is organized as follows. The anisotropic RBF interpolation is analyzed from a spectral point of view in Sect. 2, while Sect. 3 introduces the adaptive anisotropic interpolation scheme. Section 4 describes the edge-driven metric used. In Sect. 5, we discuss the main issues of the anisotropic RBF algorithm applied to the image interpolation problem. In Sect. 6 we illustrate the results obtained by the proposed algorithm, providing a comparison with well established interpolation methods.

2 Anisotropic RBFs: A Spectral Characterization

In this section we will characterize the anisotropic RBFs in terms of their spectrum and error estimation for interpolation. This will provide us with a strong motivation for using them as key ingredients in the local interpolation method introduced in Sect. 3.

The anisotropic RBFs were introduced in [4] in the context of shape preserving surface reconstruction, and further investigated in [5] as concerning their regularizing property.

The *anisotropic radial basis function* represents a deformation of the corresponding isotropic RBF as is stated in the following definition.

Definition 1 Given a set of N pairwise distinct points $X = \{\mathbf{x}_j \in \mathbb{R}^d\}_{j=1,\ldots,N}$ (denoted by *centers*), and a $d \times d$ symmetric positive definite matrix T, the *anisotropic radial basis function* associated with a radial basis function $\Phi_j(\cdot) = \varphi(\| \cdot - \mathbf{x}_j\|_2)$ is defined by

$$\Phi_{T,j}(\cdot) := \varphi(\| \cdot - \mathbf{x}_j\|_T), \tag{8}$$

where $\|\mathbf{x}\|_T = \mathbf{x}^T T \mathbf{x}$. In other words it is a function whose level sets are hyper-ellipsoids, centered in $\mathbf{x}_j$, and associated with the quadratic form $(\mathbf{x} - \mathbf{x}_j)^T T (\mathbf{x} - \mathbf{x}_j)$.

The anisotropic RBFs are no longer radial with respect to the Euclidean norm, but can be considered radial with respect to the new metric T. The strict relationship between the anisotropic RBFs and their isotropic counterparts is highlighted by the following spectral characterization, provided, for simplicity's sake, for $d = 2$.

Proposition 1 *Let* $\widehat{\Phi}(\omega) = \widehat{\varphi}(\|\cdot\|_2)$ *be the generalized Fourier transform of* $\varphi(\| \cdot \|_2)$, *and* T *a given symmetric* 2×2 *positive definite matrix with eigenvalues* λ_1, λ_2, *then*

$$\widehat{\Phi_T}(\omega) = \frac{1}{\lambda_1 \lambda_2} \widehat{\varphi}(\|\cdot\|_{T^{-1}}) \tag{9}$$

is the generalized Fourier transform of Φ_T *defined in* (8).

Proof The matrix T can be factorized as $T = M^T M$, where $M = \Lambda R$, where $\Lambda = \begin{bmatrix} \sqrt{\lambda_1} & 0 \\ 0 & \sqrt{\lambda_2} \end{bmatrix}$ is the diagonal eigenvalue matrix, and R is the orthogonal eigenvector matrix. These matrices represent respectively an anisotropic scaling matrix and a rotation matrix. Since $T = R^T \Lambda^2 R$, then $T^{-1} = R^T (\Lambda^2)^{-1} R$, then, using the scaling and rotation properties of the Fourier transform, relation (9) is established. $\square$

Since M represents an affine transformation, it follows that replacing the Euclidean norm by the T-norm corresponds to applying the Euclidean norm to a deformed spatial domain. In fact,

$$\|\mathbf{x}\|_T = \sqrt{\mathbf{x}^T T \mathbf{x}} = \sqrt{\mathbf{x}^T M^T M \mathbf{x}} = \|M\mathbf{x}\|_2. \tag{10}$$

Proposition 1 highlights that the deformation in the spatial domain produces a corresponding deformation in the frequency domain. This is illustrated in Fig. 1 where an inverse multiquadric RBF together with its Fourier transform (left) is shown. Deformations in the frequency and spatial
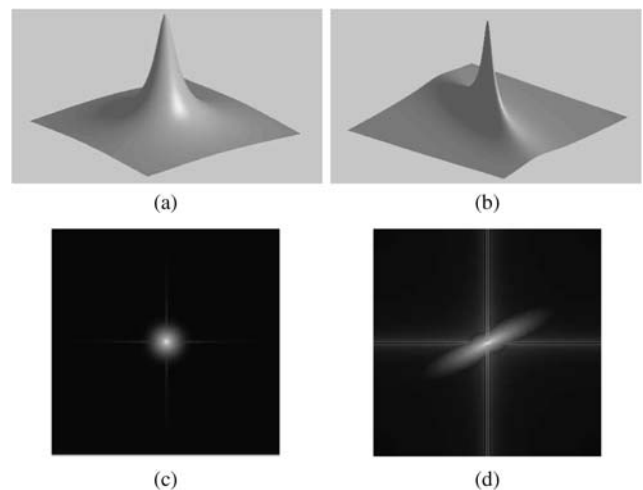
Fig. 1 (**a**) Inverse multiquadric RBF; (**b**) Anisotropic inverse multiquadric RBF; (**c**) Fourier transform of the inverse multiquadric RBF; (**d**) Fourier transform of the anisotropic inverse multiquadric RBF

domains for the associated anisotropic inverse multiquadric RBF are shown in Fig. 1(right) for a given T metric.

The spectral characterization of the anisotropic RBFs provides us with a tool to investigate their interpolation capabilities.

The anisotropic RBF interpolation to the points $(X, f) \in \mathbb{R}^{d+1}$ using the new basis functions is constructed by replacing in (6) the matrix A with $A_T = (\varphi(\|\mathbf{x}_i - \mathbf{x}_j\|_T))_{i,j=1,...,N}$, and solving the linear system

$$A_T \mathbf{c} = \mathbf{f}. \tag{11}$$

The unique solvability of the linear system (11) is guaranteed by the following result, which generalizes to the associated anisotropic $\Phi_{T,j}(\cdot)$ the definition of *positive definite function* for $\Phi_j(\cdot)$.

Proposition 2 *Given a positive definite radial function* $\Phi : \mathbb{R}^d \to \mathbb{R}$, *and a* $d \times d$ *symmetric, positive definite matrix* T, *then for all sets of pointwise distinct centers* $X \subseteq \mathbb{R}^d$, *the matrix* $A_T = (\varphi(\|\mathbf{x}_i - \mathbf{x}_j\|_T))_{i,j=1,...,N}$ *is symmetric and positive definite, namely* $\Phi_T : \mathbb{R}^d \to \mathbb{R}$ *is positive definite.*

Proof According to (10), the solution of the linear system (11), computed on the original data set X in $\mathbb{R}^d$, is equivalent to the solution of (6) on the transformed data set $Y = MX$ in $\mathbb{R}^d$, where M is the non singular matrix such that $T = M^T M$. Hence $A_T = (\varphi(\|\mathbf{y}_i - \mathbf{y}_j\|_2))_{i,j=1,...,N}$, where $\mathbf{y}_i \in Y$; then A_T is positive definite due to the positive definiteness of the considered radial basis function. $\quad\square$

Due to the shown spectral properties of the anisotropic RBFs, the anisotropic interpolant

$$F_T(\mathbf{x}) = \sum_{j=1,...,N} c_j \varphi(\|\mathbf{x} - \mathbf{x_j}\|_T), \tag{12}$$

allows a better fitting of the data with respect its isotropic counterpart. In order to give a theoretical justification, we introduce a suitable reproducing-kernel Hilbert space, which is always generated by any positive definite radial function $\Phi(x) = \varphi(\|\mathbf{x}\|)$ on a domain Ω, named *native space* of the $\Phi(x)$ function. In the isotropic case the following result holds [16].

Proposition 3 *Any translation-invariant Hilbert subspace of* $L_2(R^d)$, *which admits continuous and linear independent point evaluation functionals, is a reproducing kernel Hilbert space of a symmetric and positive definite* L_2 *function* $\Phi : \mathbb{R}^d \to \mathbb{R}$, *and can be written as a space*

$$H_\Phi = \left\{ f \in L_2(R^d) : \int \frac{|\widehat{f}(w)|^2}{\widehat{\Phi(w)}} dw < \infty \right\}. \tag{13}$$

In other words, the native Hilbert space H_Φ, contains the functions f which are *dominated* by the function Φ. Similarly, we can define the native space of the anisotropic RBF Φ_T on $\mathbb{R}^d$ as follows

$$H_{\Phi_T} = \left\{ f \in L_2(R^d) : \int \frac{|\widehat{f}(w)|^2}{\widehat{\Phi_T(w)}} dw < \infty \right\}. \tag{14}$$

The native space H_{Φ_T} represents an extension of the space H_Φ, which reduces to H_Φ when T is the identity matrix. Furthermore, we note that, while the space H_Φ is invariant under translation and rotation in $\mathbb{R}^d$, H_{Φ_T}, due to its anisotropic nature, is only a translation-invariant subspace of $L_2(R^d)$.

We will now exploit the more general nature of the native space H_{Φ_T} to explain the improved approximation capabilities of the interpolant (12). Assume that the function f belongs to the native space of the radial basis function Φ, a bound for the local error $f(\mathbf{x}) - F(\mathbf{x})$ is given by

$$|f(\mathbf{x}) - F(\mathbf{x})| \leq P(\mathbf{x}) \|f\|_{H_\Phi} \tag{15}$$

where $P(\mathbf{x})$ is the power function [17].

When the function f is characterized by high frequency components, in order to make use of (15), we are forced to choose small shape constants for inverse multiquadrics and Gaussian, so that the generalized Fourier transform contains the same high frequencies as $\widehat{\Phi}$. However, as shown in Table 1 in [16], decreasing the shape constants makes the lower bound of the power function increase and, at the same time, produces a worse reconstruction.

Instead, if we use the anisotropic RBFs Φ_T, their native space H_{Φ_T} contains the f itself, that is, the relation

$$\|f\|^2_{H_{\Phi_T}} := \frac{1}{(2\pi)^d} \int \frac{|\widehat{f}(w)|^2}{\widehat{\Phi}_T} dw < \infty \tag{16}$$

holds, without the need to act on the shape constants. In this case, the upper bound of the local error reconstruction of type (15) can be reduced.

The above considerations have motivated our proposal for an adaptive interpolation method applied to the image interpolation problem. In this case, f represents a bivariate continuous intensity function, and the high frequency components characterize the image 'edges'. We want to recover this function preserving such 1D structures. To this aim, we use the new metric T to deform the function Φ_T, in the spatial domain, along the 1D structure and, in the frequency domain, orthogonally to the 1D structure. Thus the corresponding generalized Fourier transform suitably fits the behavior of the spectrum of the function to be recovered. This deformation guarantees a better reconstruction of the function without any drastic changes in the shape constant value of Φ_T, even if, so far, a sharp bound for the local interpolation error in the case of anisotropic RBFs is not yet available.
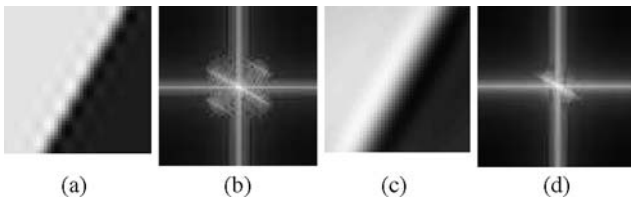
Fig. 2 (**a**) Inverse multiquadric RBF reconstruction; (**b**) Fourier transform of the reconstruction; (**c**) Anisotropic inverse multiquadric reconstruction; (**d**) Fourier transform of the anisotropic reconstruction

To support the above theory, in Fig. 2 we show the recovery of a function representing an oblique edge. In Fig. 2(a) the reconstruction on 6400 points is obtained by solving an interpolation problem on a data set X of 400 points using inverse multiquadric RBFs, while the reconstruction in Fig. 2(c) has been obtained using anisotropic RBFs Φ_T with shape constant $\gamma = 0.1$, as in the isotropic case. The anisotropic reconstruction better captures the 1D structure of the function f, while the restored function determined with the isotropic RBF interpolant shows artifacts and a poorly defined edge. Moreover, Fig. 2(b) and Fig. 2(d) provide a qualitative comparison of the Fourier transform image spectra of the reconstructed images, by isotropic and anisotropic RBF interpolants, respectively. Fig. 2(d) shows a spectrum shape prolonged similarly to the spectrum of the original function f, while the Fourier transform in Fig. 2(b) of the isotropic reconstruction shown in Fig. 2(a) presents spurious frequencies which lead to a staircase reconstruction of the edge.

An arbitrary function f is, in general, characterized by many different 1D structures. If we want to solve the interpolation problem globally, that is by solving a unique large linear system in form (6), since different 1D structures lead to different deformations of the anisotropic RBFs, the interpolation matrix could not longer be symmetric and definite. Consequently, the unique solvability of the interpolation process cannot be guaranteed. In the next section we show how to overcome this problem by combining different small anisotropic contributions to obtain a feature-preserving reconstruction of the whole f function.

3 RBF Adaptive Anisotropic Interpolation

An RBF local interpolation method has been proposed in [12] as useful approach to the reconstruction of unstructured data sets. In [3] and [4] the RBF interpolation method has been proposed for the reconstruction of large data sets exploiting the local nature of the method. This approach is based on the subdivision of the global domain Ω into smaller overlapping domains $\{\Omega_j\}_{j=1,\dots,N}$, where the RBF interpolation problem is solved locally. Non-negative weight functions $\{W_j\}_{j=1,N}$, with limited support $supp(W_j) \subseteq \Omega_j$, are

associated with this covering. Then a linear weighted combination of local solutions is constructed, using these weighting coefficients to obtain a smooth, locally defined global interpolant.

The local setting of the RBF method, which has been introduced to overcome the well-known problem of ill-conditioning, arising in the global RBF interpolation [16], now turns out to be an optimal solution to match the different behaviors of arbitrary functions.

We are now strongly motivated to combine the local interpolation approach with the adaptive anisotropic RBF interpolants which locally capture and preserve the several 1D structures of the function to be reconstructed. Without loss of generality, we consider that the compact set $\Omega = [1, n_1] \times [1, n_2] \subset \mathbb{R}^2$, the set of distinct nodes $p := (i, j)$, $i = 1, \dots, n_1$, $j = 1, \dots, n_2$, $p \in \Omega$, and the set of the corresponding image integer values U_p are given. For each p, we associate a symmetric positive definite matrix T_p and a set $NQ\_neigh(p)$ containing $NQ - 1$ *suitable* T_p-neighbors of p, as well as p itself. The term T_p-neighbors denotes that the distance is measured using the norm induced by T_p. The nodal anisotropic RBF interpolant associated with p on the set $NQ\_neigh(p)$, is defined as

$$F_{T_p}(\mathbf{x}) = \sum_{\overline{p} \in NQ\_neigh(p)} c_{\overline{p}} \varphi(\|\mathbf{x} - \overline{p}\|_{T_p}), \qquad (17)$$

where $\varphi(\cdot)$ are positive definite radial basis functions.

The coefficients $c_{\overline{p}}$ in (17) are computed by solving the linear system

$$F_{T_p}(\overline{p}) = U_{\overline{p}}, \quad \forall \overline{p} \in NQ\_neigh(p),$$

which is uniquely solvable.

Moreover, for each $p \in \Omega$, we identify an ellipsoidal region of influence Ω_p, centered in p, defined as

$$\Omega_p := \{\mathbf{x}; \|\mathbf{x} - p\|_{T_p} < \rho_p\}$$

where ρ_p is suitably chosen so that the union of the $n_1 \cdot n_2$ sets Ω_p represents a covering of Ω.

The evaluation of the *global adaptive anisotropic interpolant* in a generic point $\mathbf{x} \in \Omega$ is then given by:

$$F(\mathbf{x}) = \frac{\sum_{p \in N_{\mathbf{x}}} W_{T_p}(\mathbf{x}) F_{T_p}(\mathbf{x})}{\sum_{p \in N_{\mathbf{x}}} W_{T_p}(\mathbf{x})}, \qquad (18)$$

where $N_{\mathbf{x}}$ is the set of indices of all the nodes p s.t. $\|\mathbf{x} - p\|_{T_p} < \rho_p$, namely, the nodes whose influence region Ω_p contains $\mathbf{x}$, and the p-th compactly supported nodal *anisotropic weight function* is defined as

$$W_{T_p}(\mathbf{x}) = \left[\frac{(\rho_p - \|\mathbf{x} - p\|_{T_p})_+}{\rho_p \|\mathbf{x} - p\|_{T_p}} \right]^2. \qquad (19)$$

The use of weighted functions W_{T_p} that are anisotropic according to the same metric T_p associated with F_{T_p}, allows us to consider as a contribution to the global interpolant only the central part of any local reconstruction F_{T_p}, which represents the best fitting. This avoids the oscillations which eventually perturb the boundary part.

The function $F(\mathbf{x})$ is a continuous interpolant that follows the local anisotropies of the data. If the data are the intensity values of a discrete $n_1 \times n_2$ image, this interpolant allows us to resize the image by an arbitrary real factor. In Sect. 5 we provide an efficient algorithm which computes $F(\mathbf{x})$ using only local evaluations.

A fundamental ingredient in this new approach is the choice of the suitable metric that models the local data anisotropy. This choice will be discussed in Sect. 4 for the specific case of image data sets.

4 Edge-driven Metric for Anisotropic Interpolation

Several image interpolation methods have shown to be quite effective, due to the fact that they incorporate the edge-structure information into the interpolation process. In general, in image processing applications, the knowledge about edge orientation is important to successfully detect high-resolution structures. As shown in Sect. 2, a tool to easily capture the edge orientation is the Fourier transform which highlights high frequencies across the edge and low frequencies along the edge. In the spatial domain, the edge orientation is well captured by the local *coherence* measure of the image structures. The coherence descriptor has been applied for the analysis of coherent flow-like structures, and it has recently become a well-known tool for image processing and texture analysis [20, 21]. From a mathematical point of view it can be accomplished in a natural way by means of the structure tensor (second-moment matrix) as follows.

Consider a rectangular image domain Ω, and let a grey-level image $I(\mathbf{x})$ be represented by a bounded mapping $I : \Omega \to \mathbb{R}$. A simple edge descriptor is then given by ∇I_σ, the gradient of a Gaussian-smoothed version of I:

$$I_\sigma := (K_\sigma * I)(\mathbf{x})$$

where $\sigma > 0$, the Gaussian constant, denotes the scale under which the details are ignored. Even if ∇I_σ is useful for detecting edges, it is unsuited to finding general structures in images, since it is not invariant to sign changes, see [20]. A better descriptor is provided by the tensor product

$$J_0(\nabla I_\sigma) := \nabla I_\sigma \otimes \nabla I_\sigma,$$

which is a symmetric and positive semi-definite matrix with eigenvectors parallel and orthogonal to ∇I_σ, respectively.

The corresponding eigenvalues $|\nabla I_\sigma|^2$ and 0 describe the contrast in the eigendirections. The structure tensor is then obtained by applying a componentwise convolution with a Gaussian K_ρ:

$$J_\rho(\nabla I_\sigma) := (K_\rho * J_0(\nabla I_\sigma)) \tag{20}$$

where $\rho \geq 0$ represents the integration scale reflecting the characteristic size of the structures. The matrix J_ρ is symmetric positive semi-definite and its eigenvalues $\mu_1 \geq \mu_2$ integrate the variation of the grey values within a neighborhood of size $O(\rho)$. They describe the average contrast in the corresponding eigendirections $\mathbf{v}_1$ and $\mathbf{v}_2$. The orientation of the eigenvector $\mathbf{v}_2$, corresponding to the smaller eigenvalue, represents the direction of lowest fluctuations, the so-called coherence orientation. In this way, constant areas are characterized by $\mu_1 = \mu_2 = 0$, while edges give $\mu_1 \gg \mu_2$.

The normalized coherence value which measures the anisotropic structures within a window of scale ρ is thus defined as

$$c = \frac{(\mu_1 - \mu_2)^2}{\max\{\mu_1, \mu_2\}}, \quad c \in [0, 1]. \tag{21}$$

In our approach we first address the problem of detecting coherent structures in images, and then we use this information to design a suitable metric which drives the RBF anisotropic interpolation.

To this aim, we define the *sharpness function* $\tau(\cdot)$ as

$$\tau(c) = e^{-c}, \quad 0 \leq c \leq 1, \tag{22}$$

for each pixel of I, and we use this function to continuously adapt the metric to the local edge strength. In fact, in order to adapt the interpolation process to the local behavior of the image, we model the anisotropy of the RBF by constructing the matrix T as a function of the local image structures. This matrix has the same eigenvectors as J_ρ and its eigenvalues are given by

$$\lambda_1 = 1, \qquad \lambda_2 = g(\tau(c)), \tag{23}$$

where $g(\cdot) : [1, e] \to [1, m], m \geq 1$, is a monotone increasing function such that $g(1) = 1$, and it suitably adapts its values to the anisotropy. Therefore,

$$T = [\, \mathbf{v}_1 \quad \mathbf{v}_2 \,] \begin{bmatrix} \lambda_1 & 0 \\ 0 & \lambda_2 \end{bmatrix} \begin{bmatrix} \mathbf{v}_1^T \\ \mathbf{v}_2^T \end{bmatrix}. \tag{24}$$

A local homogeneous area of an image, named isotropic region, is characterized by a sharpness function $\tau(0) = 1$, and therefore the T-metric is reduced to be the Euclidean metric, while areas with strong edges are characterized by $\tau(1) = e$ and by a $g(\cdot)$ function which can emphasize the anisotropy. According to the choice of $g(\cdot)$, this can guarantee that the continuity of the sharpness function carries over

to the anisotropic interpolation process. We will describe our choice of $g(\cdot)$ in Sect. 6.

Remark Using an RBF interpolant, the reconstruction quality is well-known to be affected by the choice of the shape parameter in the definition of the RBF, such as γ for the inverse multiquadrics in (4). The choice of this parameter value represents a critical problem in RBF interpolation which, so far, has no optimal solution. We can exploit the role of the sharpness function to estimate a suitable γ value to model the shape of the basis functions according to the local anisotropy. We can choose to set up a new γ_τ proportional to the sharpness function as follows:

$$\gamma_\tau = \gamma \frac{1}{\tau^2}.$$

This choice has worked well for the numerical tests where each local interpolation uses data scaled on the domain $[0, 1]^2$ and $\gamma = 1$.

In a similar way the shape parameter α in (5) for a Gaussian RBF can be suitably adapted to obtain an edge-driven reconstruction.

5 Anisotropic RBF Enlargement Algorithm

In this section we present an algorithm for an arbitrary enlargement of a given input image U based on the global adaptive RBF interpolation scheme described in Sect. 3.

We suppose that in a general application setting the original and the desired image resolutions are given and we can even ignore the enlargement factor. The input image U of size $n_1 \times n_2$ is thus scaled into the target image V of size $N_1 \times N_2$, so that the scaling factor $s = (s_1, s_2)$ is given by $s_1 = N_1/n_1$ and $s_2 = N_2/n_2$.

The ARBF enlargement algorithm is based on the computation of a real bivariate function $F : \Omega \to \mathbb{R}$, which interpolates the values of the image U. This function is then evaluated on the $N_1 \times N_2$ finest grid in Ω of points $\mathbf{x} = (x, y)$, where $\mathbf{x} = (\frac{i}{s_1}, \frac{j}{s_2})$, $i = 1, \ldots, N_1$, $j = 1, \ldots, N_2$. At each point $\mathbf{x}$ corresponds a pixel $\mathbf{q} := (i, j)$, $i = 1, \ldots, N_1$, $j = 1, \ldots, N_2$ on the finest grid. The values V_q, obtained evaluating the associated points $\mathbf{x}$, represent the grey-level intensities of the enlarged image V.

The main steps of the algorithm are the following. The preliminary STEP 1 computes and stores the coherence values as in (21), by means of the structure tensor, for each pixel $\mathbf{p} \in U$. These coherence values are then used in STEP 2 to construct the matrix $T_\mathbf{p}$ defining the metric for each pixel $\mathbf{p} \in U$. We observe that the matrix $T_\mathbf{p}$ does not need to be stored. Moreover, in STEP 2, for each pixel $\mathbf{p} \in U$, we set up all the required information used to perform the local

interpolation (STEP 2.1) and we evaluate (STEP 2.2) the local interpolant in all the points $\mathbf{x}$ of the refined grid that belong to its influence region, together with the associated weights. This avoids the storing of all the interpolation coefficients. In this way, for all the points in the refined grid all the weighted local contributions are summed up. In the final step (STEP 3), all the accumulated local contributions are finally normalized according to (18).

Fig. 3 Image interpolated by the ARBF algorithm using a scaling $\times 4$ of a 128×128 original image; some circular and ellipsoidal Ω_p regions are shown

---

Algorithm 1 ARBF enlargement algorithm

INPUT: U image of size $n_1 \times n_2$, size N_1, N_2 for V
OUTPUT: V image of size $N_1 \times N_2$
$s_1 = N_1/n_1, s_2 = N_2/n_2$
STEP 1 Compute the sharpness function $\tau()$ for each pixel
      of U
STEP 2 For each pixel $\mathbf{p}$ in U
      Compute the metric $T_\mathbf{p}$
      Compute $NQ\_neigh(\mathbf{p})$ in U according to $T_\mathbf{p}$
      Evaluate ρ_p to identify Ω_p
      STEP 2.1 Local Interpolation:
      Compute $F_{T_p}(\cdot)$ by (17)
      STEP 2.2 Evaluation:
      Compute the set $Q_p = \{\mathbf{x} \in \Omega_p\}$
      For each $\mathbf{x}$ of Q_p
          $V_q = V_q + F_{T_p}(\mathbf{x})W_{T_p}(\mathbf{x})$
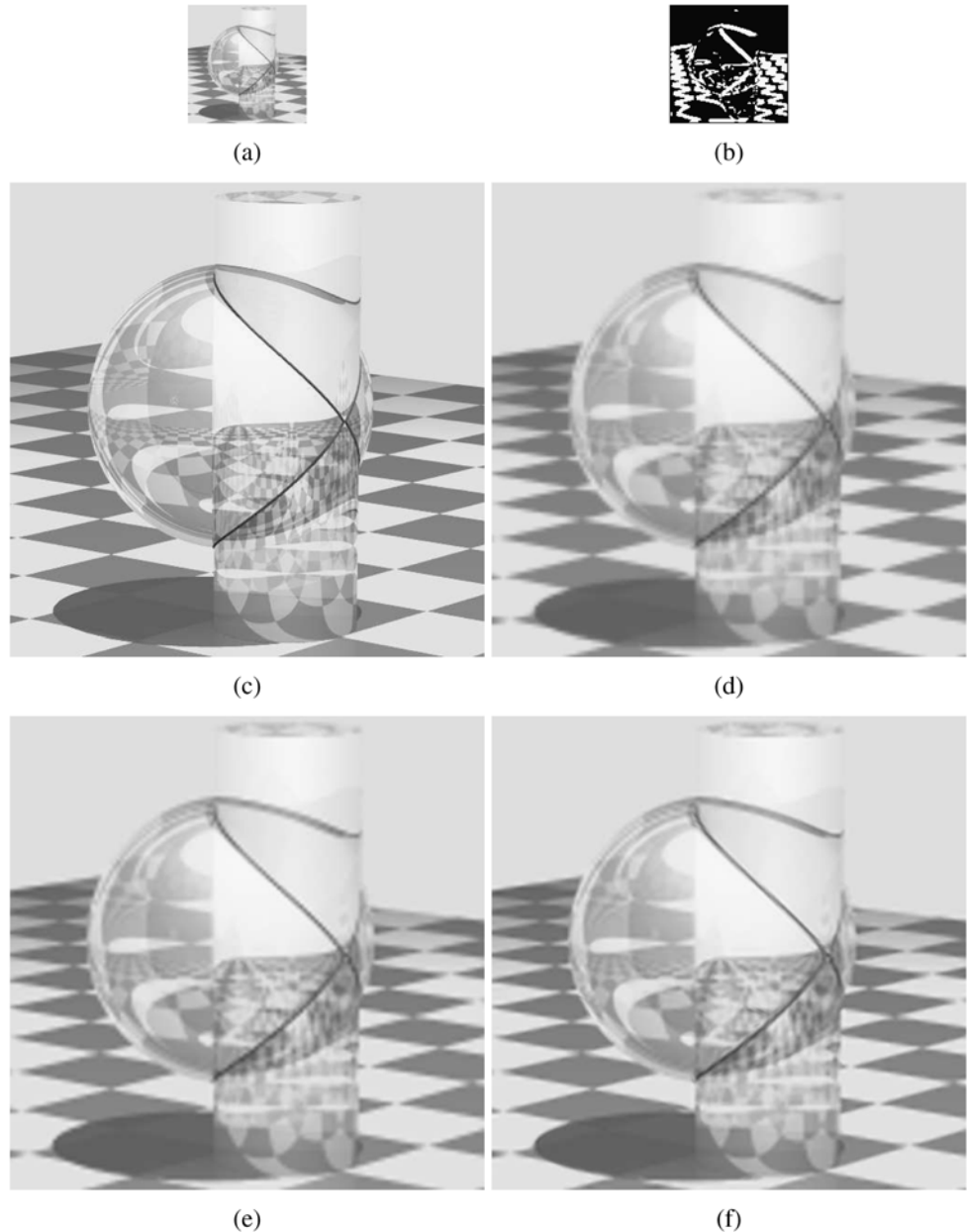 $Z_q = Z_q + W_{T_p}(\mathbf{x})$
      end for
end for
STEP 3 For each point $\mathbf{x}$ on the finest grid
         $V_q = V_q/Z_q$
end for

Fig. 4 Enlargement ×4 of
`viviani` image, $\overline{c} = 0.005$:
(**a**) 128 × 128 initial image
(**b**) coherence map
(**c**) 512 × 512 original U_0 image
(**d**) bilinear interpolation
(**e**) bicubic interpolation
(**f**) ARBF interpolation

(a)

(b)

(c)

(d)

(e)

(f)

Remark 1 Since we want to guarantee that the union of the subdomains Ω_p represents a covering of Ω, we can simply define Ω_p by choosing

$$\rho_p \geq \max_{\overline{p} \in I_p \cap \Omega} \|\overline{p} - p\|_{T_p}$$

where $I_p = \{(i+1, j), (i-1, j), (i, j+1), (i, j-1)\}$.

In Fig. 3 a 512 × 512 image reconstruction is shown to illustrate the adaptivity of the proposed ARBF algorithm. Some circular and ellipsoidal regions of influence Ω_p are shown in Fig. 3. They are used to consider only the central part of $F_{T_p}(\cdot)$ (see the local interpolation step in the ARBF enlargement algorithm). Fig. 3 emphasizes the capacity of

capturing the local behavior of the image in a given pixel **p**, using the metric T_p: the method uses circular regions Ω_p in correspondence of flat areas, while differently shaped ellipsoidal regions are used around the edges.

Remark 2 A simplified version of the ARBF algorithm can be obtained replacing the T_p metric by the classical Euclidean norm. This leads to a reduction in the computational cost but we loose the improvements in the reconstruction of the image features. This suggests an hybrid approach to achieve a better tradeoff between visual quality and computational complexity. An ARBF interpolation is applied only for pixels around edges identified by the sharpness function $\tau(\,)$,

Fig. 5 Enlargement ×4 of
clocks image, $\overline{c} = 0.00125$:
(**a**) 128 × 128 initial image
(**b**) coherence image
(**c**) 512 × 512 original U_0 image
(**d**) bilinear interpolation
(**e**) bicubic interpolation
(**f**) ARBF interpolation
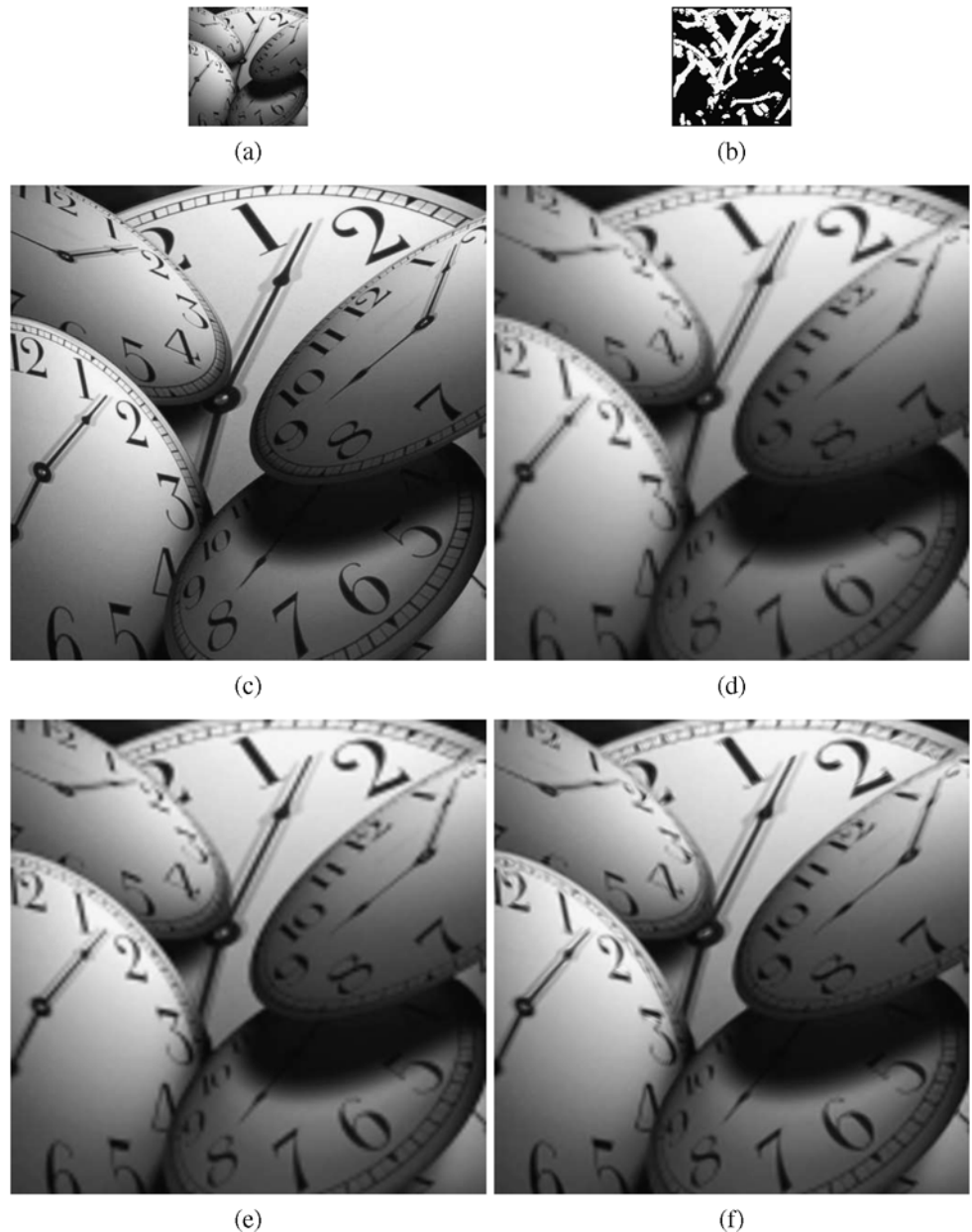
while the simplified RBF interpolation is employed elsewhere.

Remark 3 A different scenario could instead require to start from a coarse resolution image U and obtain several images V with different resolutions. In this case, instead of applying the ARBF algorithm for every enlarged V, it is certainly more efficient to compute and store the coefficients of every local interpolant for each $p \in U$, and then evaluate, for each different enlargement factor, the associated interpolated image V.

Remark 4 In [6] an anisotropic edge-enhancing strategy is applied as a post-process of linear image zooming meth-

ods. This approach could suggest to interpolate the image by standard bilinear/bicubic interpolation and then post processing the interpolated image by the anisotropic diffusion proposed by [20]. This procedure differs from the proposed ARBF interpolation process for computational effort and quality results. In fact, a post-process requires a much more computational expensive work since the structure tensor is determined for each pixel in the enlarged image and the anisotropic PDE model is then solved on the same domain. Moreover, the edge diffusion process enhances the ringing artifacts produced by a poor linear/bicubic interpolation and is not able to preserve the details that the poor interpolation has suppressed.

Fig. 6 Enlargement ×4 of
`lena` image, $\bar{c} = 0.0125$:
(**a**) 128×128 initial image
(**b**) coherence map
(**c**) 512×512 original U_0 image
(**d**) bilinear interpolation
(**e**) bicubic interpolation
(**f**) ARBF interpolation

(a)

(b)

(c)

(d)

(e)

(f)

6 Numerical Results

In this section we compare the results obtained by using the
ARBF enlargement algorithm with those obtained by the
bilinear and the bicubic interpolation methods. In order to
judge the magnification quality and analyze the reconstruction errors, we use a fine resolution image U_0 to generate a
lower resolution version U of it. Then we apply a method to
enlarge U and compare the enlarged image V with the fine
resolution image U_0. This seems to be a reasonable way to
measure the reconstruction quality.

To validate our algorithm we have chosen several alternative quantitative measurements related to picture quality
widely used in the literature. In particular, to assess the
quality of the reconstruction we have used both the Peak
Signal-to-Noise Ratio (PSNR) and the Percentage Edge Error (PEE), which are functions of the original image U_0 and
the reconstructed image V.

The PSNR measure is given by

$$PSNR(U_0, V) = 20 \log_{10} \frac{255}{RMSE(U_0 - V)} dB, \qquad (25)$$

where *RMSE* is the root mean squared errors. The PSNR is
widely used in image processing to evaluate reconstructed
image fidelity. Since it is well known that the PSNR does
not necessarily reflect the observer's visual perception of the
reconstruction, the PEE is used to measure the goodness of
the edge reproduction in the interpolated image.

According to [9] the PEE is defined by

$$PEE(U_0, V) = \frac{ES(U_0) - ES(V)}{ES(U_0)} \times 100, \qquad (26)$$

where $ES(U_0)$ and $ES(V)$ are the edge strengths of the original image and interpolated image, respectively, and it has been computed by the Euclidean norm of the gradient of the image, approximated by a central finite difference second order scheme. The PEE measures how close the interpolated image details are to the original image. A PEE positive value means that the interpolated image is over-smoothed, while negative values reveals the presence of spurious edges in the interpolated image. Due to the discrete approximation used to compute the PEE measure, it does not always express a right visual quality. The optimal quantitative measurements to capture the visual quality of the results are still an open problem.

To better appreciate the effects of the RBF anisotropic method we have considered both images with sharp edges and high local contrast and photograph-like images. The reported examples give us a qualitative and quantitative comparison on four images labelled by viviani, clocks, lena and A-char.

High quality images U_0 of size 512×512 are considered for each numerical example. The initial images U to be enlarged are obtained by the original images U_0 using the resize tool of GIMP (the GNU Image Manipulation Program). An initial image of 256×256 has been generated to produce an interpolated image by an enlargement factor $(EF) = \times 2$; when $EF = \times 4$ the initial image presents a size of 128×128 pixels, while when $EF = \times 8$ the initial image is defined by 64×64 pixels.

The ARBF algorithm can be applied to obtain arbitrary resolution enhancements, even if the reported examples consider only positive integer values for s_i, with $s_1 = s_2, s_i > 1$.

For each example, we show the coherence map associated with the image U that has to be enlarged. The coherence map is a binary image obtained by thresholding the coherence values obtained for U with respect to the $\bar{c}$ value. Our numerical tests has been performed with values of $\bar{c}$ ranging from 0.00125 to 0.05. The regions affected by the anisotropic approach correspond to white pixels in the coherence map.

In order to reduce the computational complexity, we consider in (23) the function $g(\cdot)$ as follows

$$g(\tau(c)) = \begin{cases} 1 & \text{if } c < \bar{c} \\ 3\tau(c) & \text{otherwise} \end{cases} \qquad (27)$$

where $\bar{c}$ is the threshold value used.

The effectiveness of the ARBF algorithm is shown by applying an enlargement factor $EF = \times 4$ to initial images U of size 128×128 for the viviani, clocks and lena images. The original U_0 images of size 512×512 are shown in
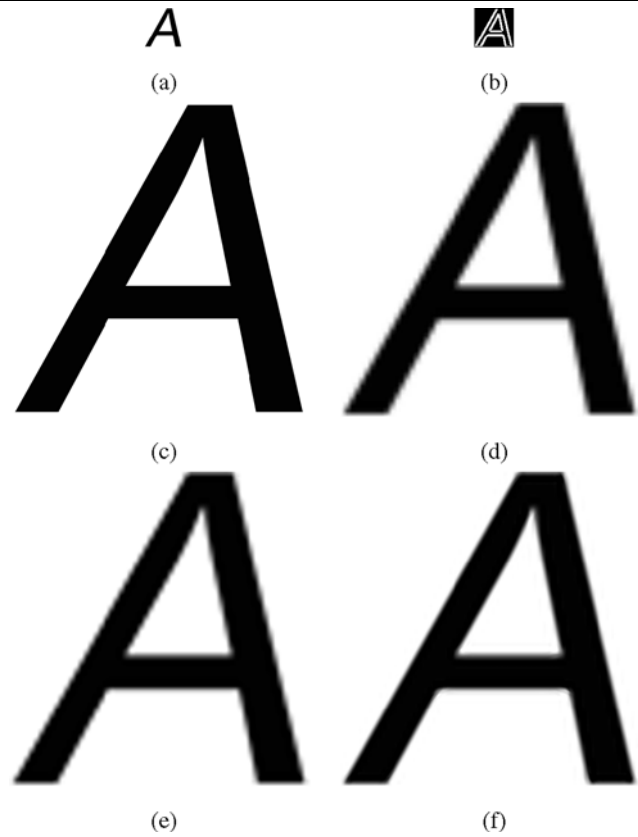

Fig. 7 Enlargement $\times 8$ of A-char image, $\bar{c} = 0.05$: (**a**) 64×64 initial image (**b**) coherence map (**c**) 512×512 original U_0 image (**d**) bilinear interpolation (**e**) bicubic interpolation (**f**) ARBF interpolation

Fig. 4(c), Fig. 5(c) and Fig. 6(c), while the enlarged V images resulting by applying the ARBF algorithm are shown in Fig. 4(f), Fig. 5(f) and Fig. 6(f). For comparison, in Fig. 4(d), Fig. 5(d) and Fig. 6(d) and Fig. 4(e), Fig. 5(e), Fig. 6(e) the interpolated images obtained by the bilinear interpolation and bicubic interpolation, respectively, are illustrated.

Figure 7 shows the results of an interpolation with enlargement factor $EF = \times 8$ of the A-char image shown in Fig. 7(a). The latter is obtained by reducing the font bitmap of size 512×512 of 256 grey-levels shown in Fig. 7(c). In this example, the image presents strong, well-defined edges separating smooth regions. We display in Fig. 7(f) the 512×512 image enlarged by the ARBF algorithm, while the images shown in Fig. 7(d) and Fig. 7(e) are obtained by applying bilinear and bicubic interpolation, respectively.

The visual quality comparison is accomplished by quantitative analysis reported in Tables 1, 2, 3, 4, where we compare the PSNR and PEE measures obtained by the ARBF algorithm for different enlargement factors (EF) with the corresponding values obtained by the bilinear (BL), and bicubic (BC) algorithms. The PSNR-values for images determined by the ARBF algorithm are the highest, and also the PEE values, in general, show a slight improvement with respect

Fig. 8 (**a**) Portion of size 64 × 64 of the clocks image of size 256 × 256; (**b**) zoom ×8 by NEDI algorithm; (**c**) zoom ×8 by bilinear; (**d**) zoom ×8 by bicubic; (**e**) zoom ×8 by ARBF interpolation, $\bar{c} = 0.005$

(a)

(b)

(c)

(d)

(e)
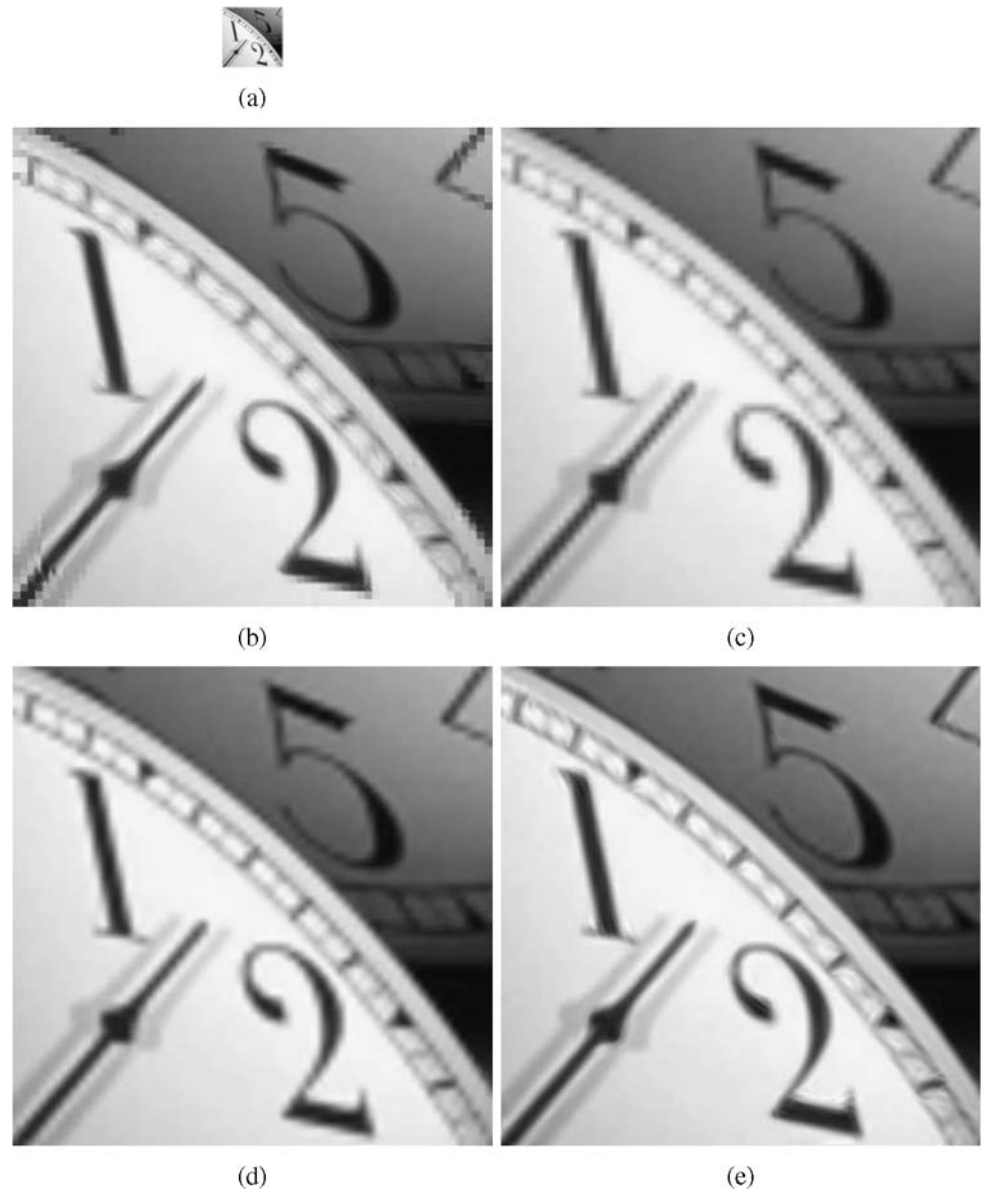
Table 1 viviani image; PSNR and PEE as function of the enlargement factor *EF* using different interpolation methods (Bilinear *BL*, Bicubic *BC*, Anisotropic RBF *ARBF*)

EF	BL		BC		ARBF	
	PSNR	PEE	PSNR	PEE	PSNR	PEE
×2	30.71	11.10	31.34	1.80	31.73	5.43
×4	25.71	35.67	26.05	28.19	26.41	23.01
×8	22.70	41.24	22.93	35.75	22.83	44.05

Table 2 clocks image; PSNR and PEE as function of the enlargement factor *EF* using different interpolation methods (Bilinear *BL*, Bicubic *BC*, Anisotropic RBF *ARBF*)

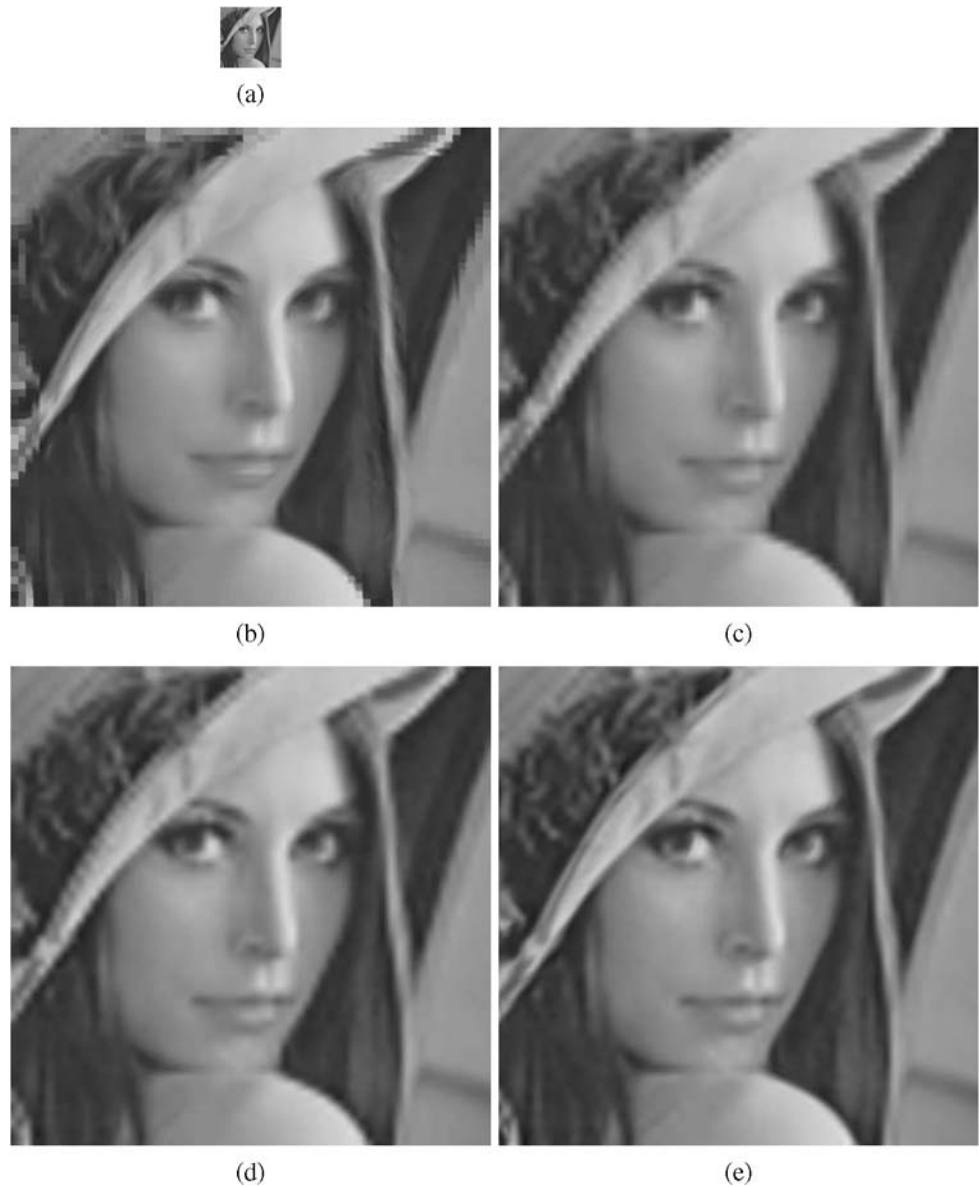| EF	BL		BC		ARBF	
	PSNR	PEE	PSNR	PEE	PSNR	PEE
×2	29.45	22.03	30.41	14.58	31.33	11.28
×4	23.75	42.08	24.17	36.03	24.50	30.85
×8	20.48	60.95	20.66	57.57	20.76	52.85

to the results obtained by the other techniques. However, what really motivates the ARBF approach, is the visual quality of the interpolated images. In particular, the ARBF approach eliminates the pixelization effects, which occur due to the variation of high-contrast areas, and it reduces the

blurring effect by sharpening the edges, resulting with visually more pleasing images. From a visual judgment the contribution of the metric T_p in the edge reconstruction using ARBF algorithm is clear, while staircase effects are still present in the linear reconstructions.

Fig. 9 (**a**) Portion of size 64 × 64 of the `lena` image of size 128 × 128; (**b**) zoom ×8 by NEDI algorithm; (**c**) zoom ×8 by bilinear; (**d**) zoom ×8 by bicubic; (**e**) zoom ×8 by ARBF interpolation, $\overline{c} = 0.0125$

(a)

(b)

(c)

(d)

(e)

Table 3 `lena` image; PSNR and PEE as function of the enlargement factor *EF* using different interpolation methods (Bilinear *BL*, Bicubic *BC*, Anisotropic RBF *ARBF*)

EF	BL		BC		ARBF	
	PSNR	PEE	PSNR	PEE	PSNR	PEE
×2	32.12	31.68	33.06	24.82	33.78	20.11
×4	27.01	49.31	27.42	44.54	27.82	40.60
×8	23.37	61.49	23.55	58.29	23.64	55.19

Table 4 `A-char` image; PSNR and PEE as function of the enlargement factor *EF* using different interpolation methods (Bilinear *BL*, Bicubic *BC*, Anisotropic RBF *ARBF*)

EF	BL		BC		ARBF	
	PSNR	PEE	PSNR	PEE	PSNR	PEE
×2	27.92	0.66	28.67	−0.75	29.89	−1.22
×4	22.90	0.93	23.26	−0.32	23.75	−2.18
×8	19.73	1.75	20.17	2.08	20.52	−0.14

We observe that all the considered interpolation algorithms have been penalized by the aliasing generated by the reduction method we applied to get U from U_0. This reduction method has allowed us to perform comparisons with the original high resolution image. However, it is not possible to perform exact recovery of an initial image from its aliased version. This problem arises when we need to represent a coarser version of an image. To overcome this problem, in the last two examples we show the results of an enlargement $EF = \times 8$ by the interpolation methods on a selected

region of size 64×64 from the original U_0 images `lena`, of size 512×512, and `clocks`, of size 256×256. The selected details are illustrated in Fig. 8(a) and Fig. 9(a). In Fig. 8(e) (Fig. 9(e)) the enlarged image V obtained by the ARBF algorithm applied to Fig. 8(a) (Fig. 9(a)) is shown. The interpolated image resulting by applying the anisotropic interpolation does not present the staircase effects clearly visible on the boundaries of the interpolated images obtained by the standard bilinear and bicubic methods illustrated in Fig. 8(c) (Fig. 9(c)) and Figs. 8(d) (Fig. 9(d)), respectively. Figs. 8(b)–9(b) include the comparison with the publicly available NEDI algorithm which implements the edge-directed interpolation method discussed in [14]; the results still suffer from noticeable artifacts and lost of details.

7 Conclusions

When linear interpolation methods are used for the image enlargement problem by a large factor, the resulting image is affected by ringing and blurring artifacts. To avoid this problems, we have presented a nonlinear interpolation method working for an arbitrary enlargement factor, which is based on the following three ingredients: the use of anisotropic radial basis functions, the introduction of a structure tensor driven metric, and the application of an adaptive anisotropic interpolation approach. An efficient combination of these ideas, has allowed us to realize a successfully interpolation method with inherent edge-enhancement properties. The various numerical examples presented show the effectiveness of the proposed approach, and the comparison with the most popular linear interpolation methods demonstrates significant improvement both on objective measures, and on visual quality of the interpolated images.

References

1. Allebach, J., Wong, P.W.: Edge-directed interpolation. Proc. IEEE Int. Conf. Image Process. **3**, 707–710 (1996)
2. Carey, W.K., Chang, D.B., Hermami, S.S.: Regularity-preserving image interpolation. IEEE Trans. Image Process. **8**, 1293–1297 (1999)
3. Casciola, G., Lazzaro, D., Montefusco, L.B., Morigi, S.: Fast surface reconstruction and hole filling using radial basis functions. Numer. Algorithms **39**, 289–305 (2005)
4. Casciola, G., Lazzaro, D., Montefusco, L.B., Morigi, S.: Shape preserving surface reconstruction using locally anisotropic RBF Interpolants. Comput. Math. Appl. **51**, 1185–1198 (2006)
5. Casciola, G., Montefusco, L.B., Morigi, S.: The regularizing properties of anisotropic radial basis functions. Appl. Math. Comput. **190**(2), 1050–1062 (2007)
6. Cha, Y., Kim, S.: Edge-forming methods for image zooming. J. Math. Imaging Vis. **25**(3), 353–364 (2006). ISSN: 0924-9907
7. Chen, M.J., Huang, C.H., Lee, W.L.: A fast edge-oriented algorithm for image interpolation. Image Vis. Comput. **23**(9), 791–798 (2005)
8. Guichard, F., Malgouyres, F.: Total variation based interpolation. Proc. Eur. Signal Process. Conf. **3**, 1741–1744 (1998)
9. Hwang, J.W., Lee, H.S.: Adaptive image interpolation based on local gradient features. IEEE Signal Process. Lett. **11**(3), 359–362 (2004)
10. Jensen, K., Anastassiou, D.: Subpixel edge localization and the interpolation of still images. IEEE Trans. Image Process. **4**, 285–295 (1995)
11. Jiang, H., Moloney, C.: A new direction adaptive scheme for image interpolation. Proc. IEEE Int. Conf. Image Process., 369–372 (2002)
12. Lazzaro, D., Montefusco, L.B.: Radial basis functions for the multivariate interpolation of large scattered data sets. J. Comput. Appl. Math. **140**, 521–536 (2002)
13. Lehmann, T.M., Gonner, C., Spitzer, K.: Survey: interpolation methods in medical image processing. IEEE Trans. Med. Imag. **18**, 1049–1075 (1999)
14. Li, X., Orchard, M.T.: New Edge-Directed Interpolation. IEEE Trans. Image Process. **10**(10), 1521–1527 (2001)
15. Malgouyres, F., Guichard, F.: Edge direction preserving image zooming: a mathematical and numerical analysis. SIAM J. Numer. Anal. **39**, 1–37 (2001)
16. Schaback, R.: Error estimates and condition numbers for radial basis function interpolation. Adv. Comput. Math. **3**, 251–264 (1995)
17. Schaback, R.: Optimal recovery in translation-invariant spaces of functions. Ann. Numer. Math. **4**, 547–555 (1997)
18. Su, D., Willis, P.: Image interpolation by pixel level data-dependent triangulation. Comput. Graph. Forum **23**, 189–201 (2004)
19. Thurnhofer, S., Mitra, S.K.: Edge-enhanced image zooming. Opt. Eng. **35**(7), 1862–1870 (1996)
20. Weickert, J.: Coherence-enhancing diffusion of colour images. Image Vis. Comput. **17**, 201–212 (1999)
21. Weickert, J., Scharr, H.: A scheme for coherence enhancing diffusion filtering with optimized rotation invariance. J. Vis. Commun. Image Represent. **13**(1/2), 103–118 (2002)

G. Casciola is Full Professor at the Department of Mathematics of the University of Bologna, Italy. He received the degree of Laura in Mathematics from the University of Bologna in 1980. The main research interests are in geometric modelling and computer graphics fields with applications to CAD/CAM systems. From 1992 he coordinated and was involved in research projects on these topics.

L.B. Montefusco received the Laurea degree in physics from the University of Bologna, Bologna, Italy, in 1969. From 1970 to 1986, she was a Researcher with the Department of Mathematics, University of Bologna. Since 1986 she has been a Full Professor. She spent some years at the University of Messina, and in 1991 she moved to the Department of Mathematics, University of Bologna, where she teaches and conducts research in the area of numerical analysis, approximation theory, digital image processing and compressed sensing. During these years she has been responsible for several Italian CNR and MURST research projects. Her research interests include approximation theory, numerical linear algebra and digital signal and image processing.

S. Morigi is an Associate Professor of numerical analysis at the Department of Mathematics, Faculty of Engineering, University of Bologna. She graduated magna cum laude in 1992, with a Laurea in computer science at the University of Bologna, Italy. In 1997 she received her PhD in applied mathematics from the University of Padova, Italy. In 1997 she did a postdoctoral fellowship at the Vanderbilt University, Tennessee, USA. Her research interests include geometric modelling, surface reconstruction, image processing and computer graphics. She is also interested in discrete ill-posed problems. She serves as a reviewer for international journals in numerical analysis and computer graphics. She has participated in several national and international research projects.